nature communications

Article

https://doi.org/10.1038/s41467-025-65513-5

First-principles full-dimensional modelling of vibrational energy transfer of molecule scattering from metal surfaces

Received: 13 April 2025

Accepted: 16 October 2025

Published online: 26 November 2025

Check for updates

Gang Meng[1,2] & Bin Jiang[1,2,3]

Energy transfer during molecular collisions on metal surfaces plays a pivotal role in a host of critical interfacial processes. Despite significant efforts, our understanding of relevant energy transfer mechanisms, even in an extensively-studied benchmark like NO scattering from Au(111), remains far from complete. To fully disentangle different energy transfer channels, we develop a first-principles nonadiabatic dynamical model that incorporates explicitly all degrees of freedom and the interfacial electron transfer. Our simulations successfully reproduce most experimental observations on vibrational relaxation and excitation of NO molecules under varying initial conditions. The observed steric effect varying with the initial vibrational state is understood by the change of orientational dependence of the metal-to-molecule electron transfer. This model also identifies that translational motion could couple to molecular vibration directly, while the translation-to-electron nonadiabatic coupling is not significant. These valuable insights highlight the importance of treating both adiabatic and nonadiabatic energy transfer pathways on equal footing, offering significant implications for modeling energy transfer processes in more complex systems, such as plasmonic photocatalysis.

Chemical reactions at metal surfaces have profound implications for interfacial applications like heterogeneous catalysis, crystal growth, and etching. Vibrational energy transfer (VET) in molecule-metal surface encounters is highly relevant to surface reactions, as molecular vibration corresponds exactly to the motion of bond breaking/forming[1–4]. Vibrational energy can be transferred to molecular translation, rotation, and surface phonons, an adiabatic process that can be described within the Born-Oppenheimer approximation (BOA)[5,6]. Beyond that, VET on metal surfaces is more complicated due to the nonadiabatic energy exchange between molecular vibration and electron-hole pairs (EHPs) of the metal, representing a breakdown of BOA[7–9]. There has been ample evidence of this nonadiabatic VET channel, causing vibrational excitation/deexcitation, electron emission, or short vibrational lifetimes[10–15]. Such nonadiabatic processes are also closely related to plasmonic catalysis, where hot electrons generated by plasmon decay may strongly couple to molecular vibration, resulting in vibrationally excited molecules that are more prone to dissociation than thermal ones[16–19]. An in-depth understanding of the VET dynamics at metal surfaces is thus highly desirable.

However, our understanding of different VET channels remains far from complete, due largely to the lack of an accurate theoretical description of both adiabatic and nonadiabatic processes on equal footing. NO scattering from Au(111) represents one of the most important examples in this aspect, attracting extensive experimental and theoretical attention[8,12,13,15,20–37]. State-to-state measurements by Wodtke and coworkers have revealed a number of fascinating features, including the multi-quantum vibrational relaxation of NO ($v_i > 0$) and its dependence on the incidence translational energy (E_i) and orientation[13,25,27,29], the vibrational excitation of NO($v_i = 0$) and its dependence on surface temperature (T_s) and E_i[15,30]. Such abundant

[1]State Key Laboratory of Precision and Intelligent Chemistry, University of Science and Technology of China, Hefei, Anhui, China. [2]Department of Chemical Physics, School of Chemistry and Materials Science, University of Science and Technology of China, Hefei, Anhui, China. [3]Hefei National Laboratory, University of Science and Technology of China, Hefei, China. e-mail: bjiangch@ustc.edu.cn

experimental data have provided detailed information on how molecular vibration couples to other degrees of freedom (DOFs), serving as valuable benchmarks to stringently test nonadiabatic theories[20–22,24,31,33,34,36–40].

Despite substantial efforts in the past two decades, no theory has so far been capable of quantitatively reproducing most experimental observations for NO collisions on Au(111)[1]. The greatest challenge is to describe the nonadiabatic interactions between the molecular states and the metallic continuum in full dimensionality. To make the simulation tractable, most theoretical studies have relied on mixed quantum-classical approaches, which treat the nuclear motion classically while electronic motion quantum mechanically. Their coupling is either addressed perturbatively on top of the ground state, as in molecular dynamics with electronic friction (MDEF)[20,33,41], or explicitly by considering two local electronic configurations as a result of electron transfer, as in the independent electron surface hopping (IESH)[21–23,37] and broadened classical master equation methods[36,42]. Fully quantum dissipative[20,40] and semi-classical[39] approaches have also been applied to this system, though limited to only two nuclear DOFs. Indeed, only MDEF and IESH models have ever been integrated with realistic full-dimensional (FD) potential energy surfaces (PESs) to enable meaningful comparisons with experimental data[15,21,33,37]. Such comparisons based on empirical PESs parameterized by Roy, Shenvi, and Tully (referred to as RST PESs hereafter) suggested an exclusive electron transfer mediated VET mechanism, which can be characterized by IESH yet not MDEF[15,23,37]. However, both methods failed to capture the translational and steric dependence of vibrational inelasticity of NO($v_i = 3$), even qualitatively[25,37,43]. These failures were attributed to the inaccuracies of the RST PESs, presumably arising from the approximate charge-transfer states and less expressive empirical functions[25,37].

More recently, we developed a more reliable ground state FD-PES by embedded atom neural network (EANN) fitting of thousands of density functional theory (DFT) data, on which Born-Oppenheimer molecular dynamics (BOMD) predicted very efficient adiabatic VET[32,35]. MDEF simulations on this PES better described the single-quantum vibrational relaxation, but still largely underestimated the extent of multi-quantum vibrational relaxation[33]. To go beyond the friction model, we applied a constrained DFT (CDFT) scheme[44,45] to determine charge-transfer (diabatic) states of molecules at metal surfaces, which was found to more reasonably describe the electron transfer between CO and NO molecules and metal surfaces[46,47]. The combination of CDFT, EANN, and IESH methods enables a first-principles description for nonadiabatic effects of molecular scattering from metal surfaces.

In this work, we demonstrate the success of this strategy in NO scattering from Au(111) using newly developed NN-based first-principles charge-transfer state PESs. With an appropriate density functional, IESH simulations on NN PESs achieved very good agreement with a wide range of experimental observations of NO on Au(111). Our results emphasize the necessity of properly characterizing both adiabatic and nonadiabatic energy transfer channels, towards a quantitative theoretical description for the VET dynamics of molecules at metal surfaces. The remaining discrepancies with experimental data are also discussed.

Results

Comparison of full-dimensional and two-dimensional dynamics

In Fig. 1, vibrational state distributions for scattered NO obtained by various levels of theory, for initial states of $v_i = 3$, 11, and 16, are compared with experiments[27,37]. For fair comparison, unless stated elsewhere, our results are analyzed based on single-bounce trajectories, consistent with prior theoretical work and the direct scattering nature of this process as observed in experiments[13]. For clarity, our results based on all trajectories are shown in Supplementary Fig. 6, and no significant differences are found.

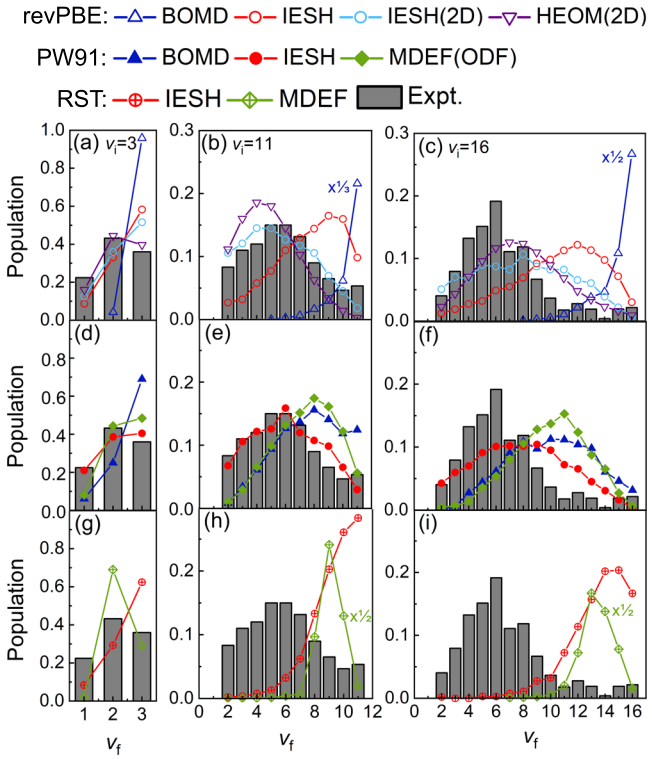

Fig. 1 | Final vibrational state distributions with various initial conditions. Comparison of experimental final vibrational state distributions[27] of vibrationally excited NO scattering from Au(111) with BOMD and IESH results on the revPBE-based FD-PESs, as well as IESH and HEOM results on the revPBE-based two-dimensional (2D)-PESs from ref. 40, for **a** $v_i = 3$, $E_i = 1.08$ eV, **b** $v_i = 11$, $E_i = 0.95$ eV, and **c** $v_i = 16$, $E_i = 0.52$ eV. **d**–**f** Similar to (**a**–**c**), but for BOMD, IESH, and MDEF(ODF)[33] results on the PW91-based FD-PESs. **g**–**i** Similar to (**a**–**c**), but for IESH and MDEF results on the RST FD-PESs from ref. 37. Note that results are extracted from trajectories with single-bounce and trajectories whose final vibrational states exceed the experimental ranges are excluded. Source data are provided in a Source data file. Results obtained from all trajectories are shown in Supplementary Fig. 6.

We first evaluate the accuracy of IESH by benchmarking IESH with a fully quantum method, namely hierarchical equations of motion (HEOM)[40,48]. Since FD HEOM simulations are currently unfeasible, we compare IESH and HEOM results based on a 2D model. As shown in Fig. 1a–c, IESH agrees well with HEOM, although the latter predicts slightly stronger vibrational inelasticity than the former in the case of NO($v_i = 3$). The good agreement between them largely validates the reliability of IESH.

To demonstrate the necessity of encompassing all DOFs in studying this energy transfer process, we also compare IESH results using 2D and FD models. As shown in Fig. 1a–c, the FD-IESH results are quite different from their 2D counterparts, manifesting much hotter vibrational state distributions for NO($v_i = 11$ and 16). Indeed, these 2D results are all based on 2D empirical PESs fitted to a limited number of CDFT points reported in ref. 46, where the NO molecule lies perpendicularly on the hcp site of Au(111) with the N atom pointing down. Electron transfer between the molecule and the surface more easily undergoes in this geometry compared to other sites and orientations (see Supplementary Fig. 7). Apparently, the effects of molecular orientation, surface site, and surface phonons are all neglected in 2D models. The large discrepancy between FD and 2D results underscores the necessity of employing FD-PESs for accurate theoretical modeling. While 2D models may coincidentally align with experimental data, our FD-IESH results remarkably underestimate the degree of vibrational relaxation, suggesting that the revPBE-based PES yields overly repulsive NO/Au(111) interactions. These findings caution against direct comparisons between

https://doi.org/10.1038/s41467-025-65513-5

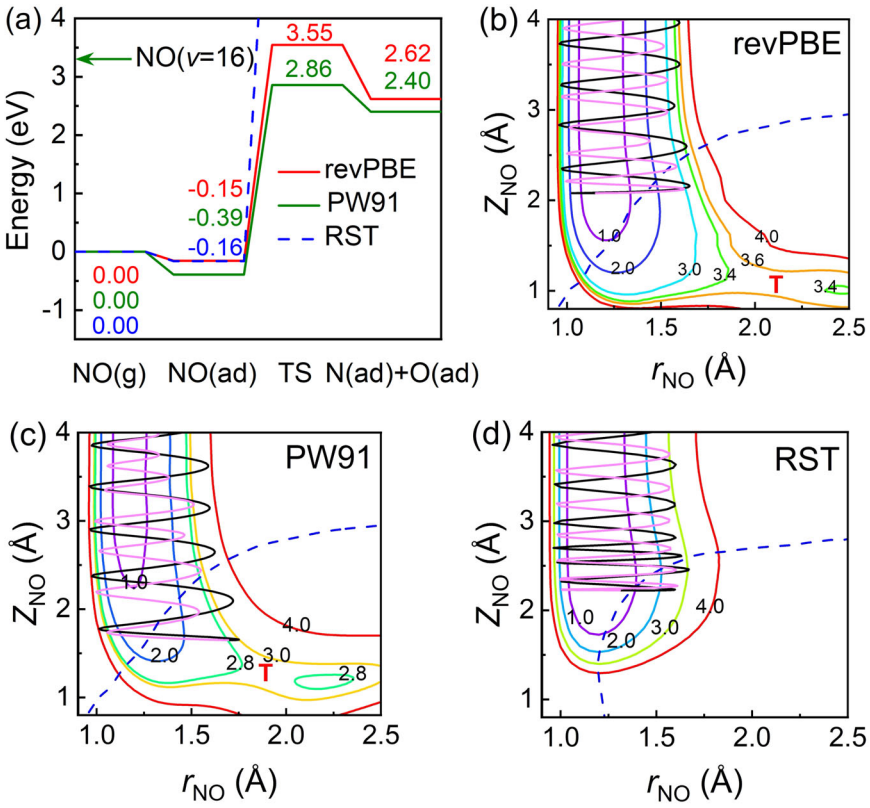

Fig. 2 | Topography of three PESs. a Comparison of energies along the minimum energy path of NO dissociation on Au(111) on the ground revPBE, PW91[35], and previous RST[23] PESs. The green arrow indicates the vibrational energy of NO($v = 16$) in our simulations. Two-dimensional cuts of the **b** revPBE, **c** PW91, and **d** RST ground state PESs as a function of r_{NO} and Z_{NO}, with two angles (θ and φ, defined in Supplementary Fig. 1) optimized and other coordinates fixed at the dissociation transition state. The energy is given relative to a free NO molecule far from the surface, in units of eV. A representative IESH trajectory, with the black line representing the incoming component and the magenta line representing the outgoing component, is projected onto the corresponding PES. The crossing seam (blue dashed line) between two diabatic states and the transition state (red "T") are also shown on the PES. Note that this crossing seam is derived from the orientation that facilitates the most efficient electron transfer, where the NO molecule is perpendicularly placed on the hcp site with the N atom pointing to the surface. Source data are provided in a Source data file.

experimental data and low-dimensional theoretical models, as the latter may fail to capture the true molecule-surface interactions and dynamics.

Influence of PES on VET dynamics

To study the influence of the PES on the adiabatic and nonadiabatic VET dynamics, we have constructed another set of FD-PESs based on the PW91 functional, where the ground state PES was reported previously[32,33,35] and diabatic state PESs are obtained in this work as described in the "Methods" section. Figure 1d–f displays results obtained on the PW91-based PESs, where MDEF results with orbital-dependent friction (MDEF(ODF)) are taken from ref. 33. As discussed previously[32,33,35], PW91-based BOMD results already predict remarkable vibrational relaxation. The MDEF(ODF) model further increases the probability of single-quantum vibrational relaxation (i.e., $\Delta v = 1$) compared to BOMD on the PW91-based PESs (Fig. 1d–f), leading to improved agreement with experimental data. However, it falls short of improving the multi-quantum vibrational relaxation (i.e., $\Delta v > 1$)[33]. Its failure was attributed to the invoked Markovian approximation, which neglects EHP excitations far away from the Fermi level[33].

Encouragingly, the IESH model, which treats both electron transfer and EHP excitations on equal footing, achieves the best agreement with experimental observations across all initial conditions to date. Quantitatively, not only does the probability of the two-quanta relaxation ($v_i = 3 \rightarrow v_f = 1$) increase remarkably, but the overall vibrational state distributions of NO($v_i = 11$ and 16) also shift to lower states, both of which align more closely with the experimental distributions. By comparing final vibrational state distributions predicted by BOMD and IESH, we conclude that adiabatic and nonadiabatic contributions to the vibrational relaxation with low and high initial vibrational states are comparable. In contrast, in Tully's work[21], they stated that the nonadiabatic channel dominates the VET for the NO/Au(111) scattering, which differs a lot from our conclusion, mainly resulting from their less accurate ground and charge-transfer state PESs.

In comparison, PW91-based results represent significant improvements over the revPBE-based and previous RST-based ones[23,37] (Fig. 1g–i). On one hand, the adiabatic VET is much more pronounced on the PW91 PES than on the other two PESs (Note that the RST-based BOMD results exhibited minimal vibrational relaxation[21], thus not shown here). This adiabatic VET arises from mode softening as the vibrating molecule approaches the dissociation barrier[32,49]. As depicted in Fig. 2, the barrier for NO dissociation on the adiabatic PW91 PES is 0.69 eV lower than that on the revPBE PES, while the RST PES is purely repulsive. In addition, the barrier locates "earlier" on the PW91 PES, featuring a shorter N–O distance, a higher molecule-surface distance, and a wider entrance to the barrier region (see Fig. 2b, c and Supplementary Table 1). These characteristics allow trajectories to access the barrier more readily on the PW91 PES, as demonstrated by an exemplary trajectory of NO($v_i = 16$) projected onto the 2D PES in Fig. 2. This facilitates significantly more efficient adiabatic VET compared to the other two PESs. On the other hand, in IESH models, the likelihood of electronic excitation is qualitatively linked to the proximity to the crossing seam between neutral and anionic states, where nonadiabatic coupling is strong and electron transfer can explicitly occur, as marked in Fig. 2 by dashed lines. Notably, trajectories on PW91 PESs are more likely to enter

https://doi.org/10.1038/s41467-025-65513-5

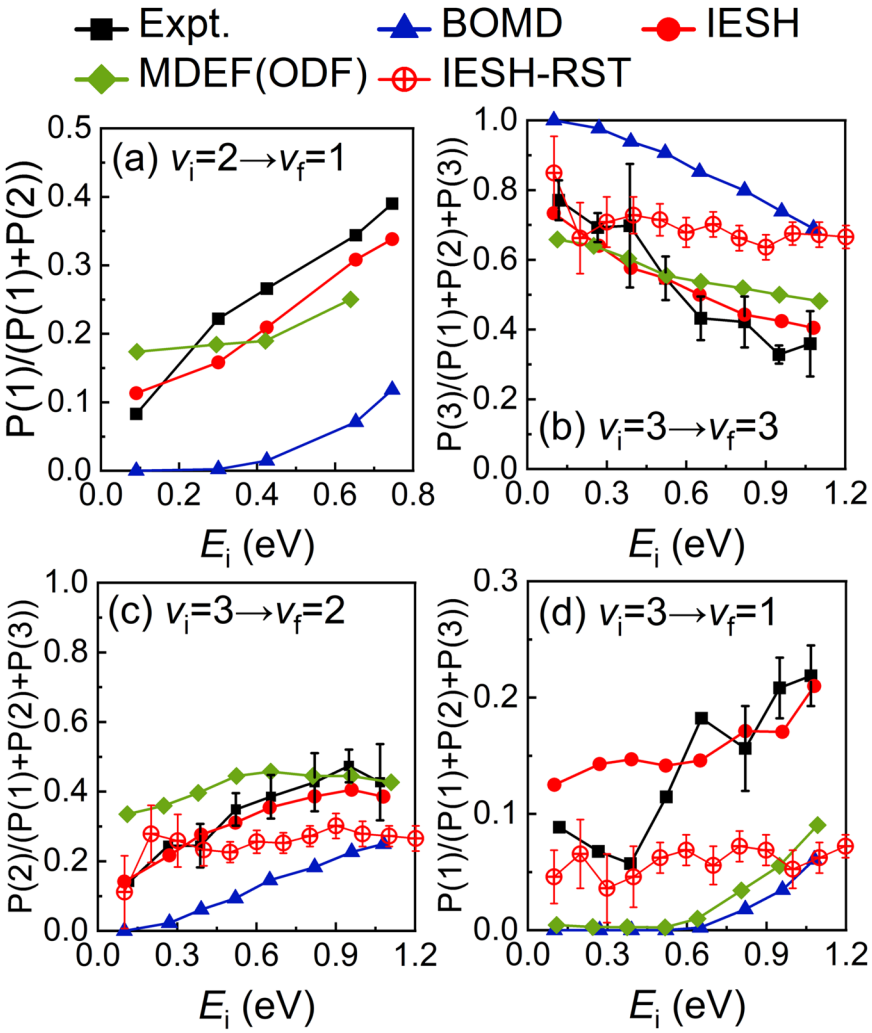

Fig. 3 | Dependence of final vibrational state distributions on E_i. Experimental branching ratios[12,25] as a function of incident translational energy E_i, in comparison with BOMD, IESH, and MDEF(ODF)[33] based on the PW91 PES and IESH using the RST PES[25], for **a** $v_i = 2$ and **b**–**d** $v_i = 3$. Note that although our calculations predict minor populations for $v_f = 0$ or $v_f > v_i$, they have not been measured in experiments, which will thus not be discussed here. Only single-bounce trajectories are included in all theoretical models, including the referenced MDEF(ODF) and IESH-RST. Error bars on the experimental data indicate statistical uncertainties originating from pulse energy fluctuations of the used lasers[25]. Error bars of IESH results based on the RST PES represent 2σ (95% confidence) statistical uncertainty[25]. Results obtained from all trajectories are shown in Supplementary Fig. 8. Source data are provided in a Source data file.

this strong-coupling region, making electron transfer possible and channeling vibrational energy dissipation into surface EHPs. Indeed, as compared in Supplementary Tables 2 and 3, the mean vibrational energy losses predicted by PW91-based PESs, due to both adiabatic and nonadiabatic channels, are larger than those predicted by revPBE-based ones. These results reveal that the PES landscape governs simultaneously both adiabatic and nonadiabatic VET channels. This is achieved by modulating the molecular accessibility to the dissociation barrier and state-crossings, which are typically located in similar regions.

Since the PW91-based IESH model appears to describe well both adiabatic and nonadiabatic VET processes, we next extend it to more comprehensive scenarios, including the dependence of vibrational relaxation probability on the incidence energy and initial orientation distribution, the vibration-to-translation coupling, and the vibrational excitation of NO($v_i = 0$). Some of these phenomena have never been adequately described by any previous theoretical models.

Incidence energy dependence of NO scattering

Figure 3 shows the experimentally measured product state branching ratios of NO($v_i = 2$ and 3) as a function of E_i. The observed vibrational inelasticity increases monotonically as E_i rises[12,25]. PW91-based BOMD results qualitatively capture this E_i-dependence, but significantly underestimate absolute ratios. MDEF(ODF) results show some improvement in the vibrationally elastic ($v_f = 3$) and single-quantum relaxed ($v_f = 2$) channels, but have a minimal impact on the two-quanta relaxed ($v_f = 1$) channel. Impressively, IESH results now well match nearly all branching ratios in the entire range of E_i, demonstrating excellent agreement with experimental data. It is easily understood that the higher incidence energy allows the NO molecule to get closer to the barrier and state-crossing point, thereby amplifying both adiabatic and nonadiabatic vibrational energy losses. In contrast, previous RST-based IESH results predict a more pronounced vibrational relaxation at lower E_i and thus much weaker E_i-dependence of the vibrational inelasticity, because of the overly softness of the RST PES.

Orientational dependence of NO scattering

An intriguing yet not fully understood experimental observation is the orientational dependence of vibrational inelasticity for the scattering

https://doi.org/10.1038/s41467-025-65513-5

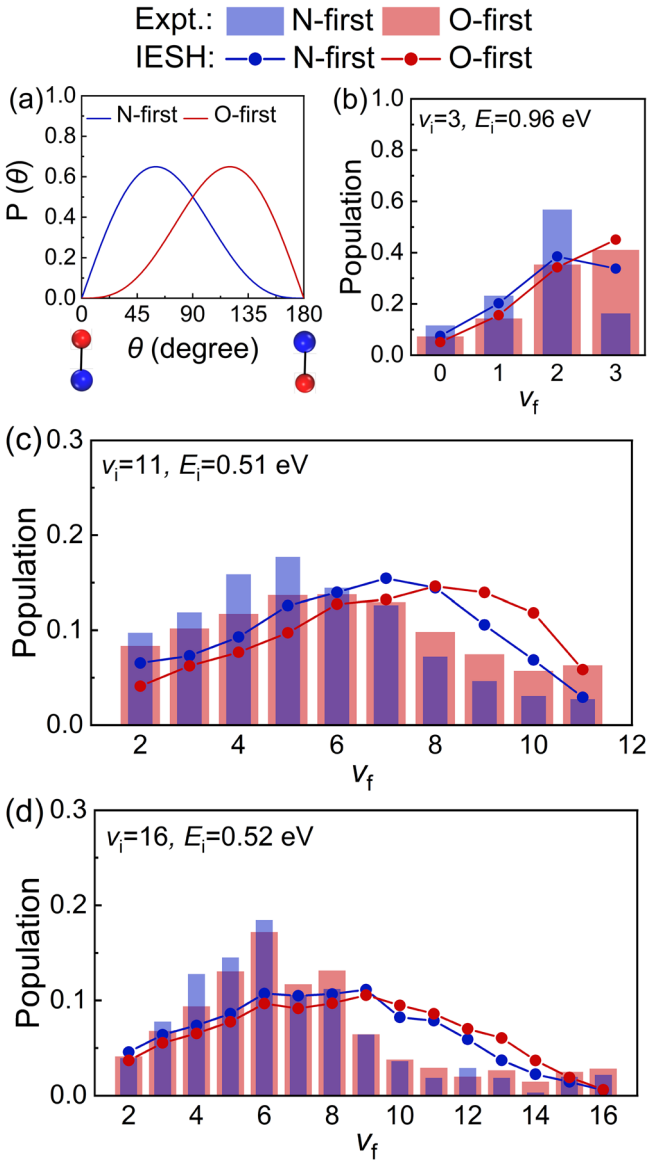

Fig. 4 | Dependence of final vibrational state distributions on initial orientation. a Initial polar angle distributions for N-first and O-first orientations of the NO molecule. Experimental final vibrational state distributions[29] of NO **b** ($v_i = 3$, $E_i = 0.96$ eV), **c** ($v_i = 11$, $E_i = 0.51$ eV), and **d** ($v_i = 16$, $E_i = 0.52$ eV) scattering from Au(111) with N-first and O-first orientations, in comparison with IESH results on the PW91 PES. Note that only single-bounce trajectories are included, and trajectories with final vibrational states beyond the experimental ranges are not included. Source data are provided in a Source data file.

of NO($v_i = 3$), which gradually diminishes as the molecule becomes more vibrationally excited[27,29]. In the experiment, the vibrationally excited NO molecule can be initially manipulated to prefer either an N-first or an O-first orientational distribution before colliding on the surface, as illustrated in Fig. 4a. Figure 4b shows that the former leads to obviously stronger vibrational relaxation than the latter during NO($v_i = 3$) scattering. However, as the initial vibrational state increases, the orientational dependence largely weakens at NO($v_i = 11$) (Fig. 4c) and nearly vanishes at NO($v_i = 16$) (Fig. 4d). Our PW91-based IESH results properly capture this steric effect and its variation with the initial vibrational state. In Supplementary Fig. 9, we further quantify the adiabatic and nonadiabatic contributions to the steric effect by comparing BOMD and IESH results with experimental data for NO($v_i = 3$). We assess the degree of vibrational relaxation using the average vibrational quantum number of scattered NO molecules, denoted as $\langle v_f \rangle$, and quantify the steric effect as the difference of $\langle v_f \rangle$ between the two initial orientations, namely $\langle v_f$(O-first)$\rangle$-$\langle v_f$(N-first)$\rangle$. A larger difference indicates a stronger steric effect. The BOMD prediction of this difference is ~0.13, suggesting a minor orientational dependence due to the adiabatic VET channel. While the IESH prediction increases this value to ~0.21, in close accord with the experimental value of ~0.23. These results demonstrate that both adiabatic and nonadiabatic channels contribute to the steric dependence of VET.

To elucidate the underlying mechanism, we first check the polar angle distributions at the impact point at which the initially N-first and O-first oriented molecules turn around (see Supplementary Fig. 10). While some O-first oriented NO molecules reorient towards the N-first orientation, the polar angle distributions in the two cases remain distinct, which is the prerequisite for the stereodynamics. However, these distributions are insensitive to the initial vibrational state, failing to explain the reduced steric effect at higher vibrational states. We then resort to searching the crossings between two diabatic state PESs, plotted as a function of Z_{NO} in Supplementary Fig. 10, with the polar angle θ fixed at 68° and 112°—values that correspond to the mean angles ($\langle\theta\rangle$) for the N-first and O-first distributions, respectively. At $r_{NO} = 1.32$ Å, approximately the outer classical turning point of NO($v = 3$), the crossing point of two diabatic states shifts to higher energies as θ increases. This indicates that N-first oriented molecules would more likely undergo charge transfer than O-first ones and experience more efficient nonadiabatic VET, consistent with their stronger vibrational inelasticity upon collisions. By contrast, when r_{NO} elongates to the turning point of NO($v = 16$), i.e., 1.59 Å, the crossings of two diabatic states become very similar in both orientations. This is in accord with the observed much weaker steric effects for high initial vibrational states. It is worth noting that previous RST-based IESH results turn out to predict no steric effect at all for NO($v_i = 3$) scattering, due to too strong dynamical steering[21,43,50] (see Fig. 4 of ref. 21 and Supplementary Fig. 10 in the Supplementary Information, which presents similar polar angle distributions at the impact point from different initial orientations).

Vibration-to-translation coupling

Dynamical results discussed have so far primarily focused on the energy exchange between molecular vibration and surface EHPs (V–EHP). However, the energy transfer process is more complex, involving other DOFs, like molecular translation and rotation. Experimental evidence suggests that the translational motion is not merely a spectator during the electronically nonadiabatic VET process, but its precise role remains elusive. For example, as shown in Fig. 5a, the mean final translational energy ($\langle E_T \rangle$) is incrementally higher in the vibrationally de-excited channels than the elastic channel[26,28]. Experimentalists have proposed two possible mechanisms: a direct mechanical coupling between vibration and translation (V–T), and/or an EHP-mediated coupling, where molecular vibration and translation do not directly couple to each other but both couple to EHPs (V–EHP and EHP–T)[26,28]. However, no theory has yet been able to determine which mechanism dominates.

Figure 5 compares the calculated and experimental $\langle E_T \rangle$ of scattered NO molecules, as a function of final rotational energy (E_R) for three product channels ($v_i = 3 \rightarrow v_f = 3, 2, 1$), at $E_i = 0.98$ eV. The experimentally observed $\langle E_T \rangle$ decreases linearly with increasing E_R for all three channels, exhibiting an anticorrelation between outbound translation and rotational excitation (T–R). In addition, the evidence of V–T energy transfer is that $\langle E_{T,vf=3} \rangle$ extrapolated to $E_R = 0$ is lower by ~0.08 eV than $\langle E_{T,vf=2} \rangle$ and ~0.12 eV than $\langle E_{T,vf=1} \rangle$, smaller than the corresponding vibrational excitation energy, respectively. In comparison, PW91-based IESH results not only correctly predict the anticorrelation between $\langle E_T \rangle$ and E_R, but also reproduce reasonably well the amount of V–T energy transfer, e.g., ~0.09 eV for $\langle E_{T,vf=2} \rangle$-

https://doi.org/10.1038/s41467-025-65513-5

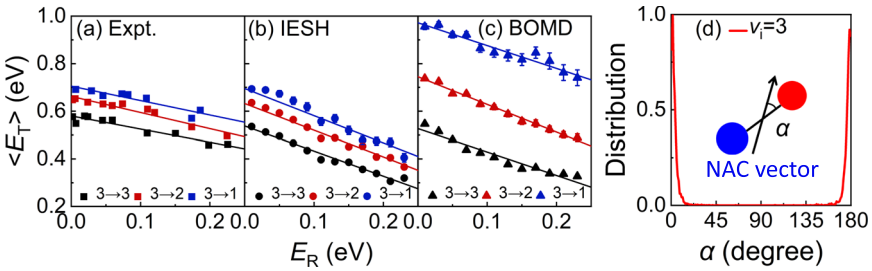

Fig. 5 | Direct vibration-to-translation coupling. a Experimental mean final translational energy[26] of the scattered NO as a function of final rotational energy for $v_i = 3 \rightarrow v_f = 3, 2, 1$ with $E_i = 0.98$ eV. **b**, **c** Same as (**a**), but calculated by IESH and BOMD on the PW91 PES. **d** Distribution of α, for which α is the angle between the nonadiabatic coupling vector and N–O bond when electronic hopping occurs in IESH. Error bars indicate standard errors. Source data are provided in a Source data file.

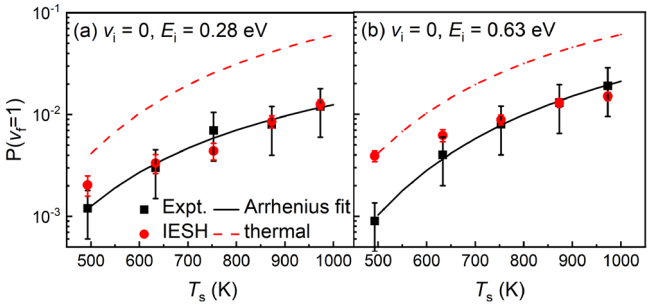

Fig. 6 | Vibrational excitation probability. Experimental vibrational excitation probability of NO($v_i = 0$) scattering from Au(111) against T_s for E_i = **a** 0.28 eV and **b** 0.63 eV[30], in comparison with IESH results on the PW91 PES. Arrhenius functions fitted to the experimental points, as well as the thermal limit, are also depicted for comparison. Error bars on the experimental data were determined by estimating the statistical uncertainties in all input variables and then calculating their propagation into the absolute excitation probability[30]. Error bars of IESH results indicate standard errors of the excitation probability. Source data are provided in a Source data file.

$<E_{T,vf=3}>$ and ~0.15 eV for $<E_{T,vf=1}>$-$<E_{T,vf=3}>$, although the slope of $d<E_T>/dE_R$ is more negative, implying the anisotropy of the entrance of the PES is less well described.

Interestingly, Fig. 5c shows that PW91-based BOMD results also exhibit a qualitatively similar anticorrelation between $<E_T>$ and E_R across three well-separated vibrational channels, suggesting a direct V–T coupling with no need to invoke nonadiabatic effects. Indeed, the differences in $<E_T>$ between adjacent vibrational channels are roughly constant at ~0.22 eV, corresponding approximately to the energy of a single vibrational quantum ($\Delta v = 1$). This means that vibrational energy can exclusively convert to the outbound translation because of vibrational deexcitation within BOA. When the nonadiabatic channel is open, part of the vibrational energy flows to EHPs, thereby reducing the differences of $<E_T>$ between vibrationally relaxed and elastic channels. This analysis also conforms to the mean energy changes in different DOFs during NO($v_i = 3$) scattering (Supplementary Table 3). Compared to BOMD, the average translational energy loss is barely changed when electronic DOFs are included via IESH, showing no evidence of energy exchange between translational and electronic DOFs. This further confirms the negligible coupling between translation and EHPs. This feature can be understood by analyzing the direction of the nonadiabatic coupling vector whenever surface hopping occurs in IESH simulations. As shown in Fig. 5d, the angular distribution between the nonadiabatic coupling vector and N–O bond (α) is sharply peaked at parallel directions, either 0° or 180°. In such scenarios, the nonadiabatic coupling vector is either parallel or antiparallel to the N–O vibrational motion, resulting in the predominance of V–EHP coupling. These results clearly demonstrate that molecular vibrational energy can transfer to both molecular translation and metallic EHPs during scattering, yet the direct T–EHP coupling is negligible, at least in the conditions considered here.

Vibrational excitation of NO($v_i = 0$) scattering

Apart from vibrational relaxation of NO at various initial conditions, vibrational excitation of NO($v_i = 0$) was also observed during its scattering from Au(111)[15,30]. In this process, the electronic energy is in turn transferred to molecular vibration. Indeed, this process is relevant to plasmonic catalysis, where nonadiabatic energy transfer from hot electrons into vibrationally excited states facilitates the bond cleavage[19]. As shown in Fig. 6, our PW91-based IESH results compare well with experimental data on the vibrational excitation probabilities for NO ($v_i = 0 \rightarrow v_f = 1$), in a range of T_s from 473 to 973 K at two representative E_i values. Both results are below the thermal limit, indicating that vibrational excitation occurs in a direct scattering process. Experimental vibrational excitation probabilities can be fitted to an Arrhenius equation on T_s. PW91-based IESH results generally follow this Arrhenius relation, except for the deviation at $E_i = 0.63$ eV, $T_s = 473$ K. The overall agreement observed here is comparable to that of the earlier RST-based IESH model[15].

Discussion

Given its significantly improved agreement with experimental results across diverse conditions compared to previous models—unlikely due to significant error cancellations—the current PW91-based IESH model represents the state-of-the-art theoretical characterization of molecule-surface scattering processes involving strong nonadiabatic effects. Despite this remarkable success, some discrepancies persist between the current theory and experiment. One deficiency is the inaccurate prediction of the molecular trapping probability. Figure 7a shows that the revPBE-based IESH model systematically underestimates the trapping probability of NO($v_i = 2$) in a range of incidence energies[51], particularly at low incident energies, whereas the PW91-based IESH model does the opposite. This discrepancy suggests that neither the revPBE-based nor PW91-based PESs are sufficiently accurate in describing molecular adsorption, with the former being likely too repulsive while the latter too attractive. Another discrepancy between theory and experiment arises in the final rotational state distributions of scattered NO($v_i = 3$), as illustrated in Fig. 7b, c. While both models capture the stronger rotational excitation for the O-first than N-first orientation in the vibrationally elastic channel, they improperly predict an artificial rotational rainbow feature for the O-first orientation in the vibrationally inelastic channel, and too much rotational excitation, especially the PW91-based IESH model. This is likely tied to the inadequate description of attractiveness, anisotropy,

https://doi.org/10.1038/s41467-025-65513-5

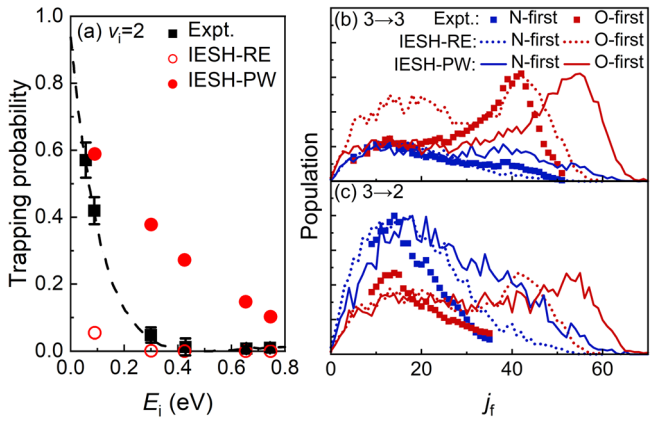

Fig. 7 | Discrepancies with experiments. a Trapping probabilities for $v_i = 2$ at a range of incident energies determined by experiments[51], compared to those predicted by IESH on the revPBE (labeled with "-RE") and PW91 (labeled with "-PW") PESs. The black dashed line represents a fit of experimentally determined trapping probabilities. Error bars represent uncertainties associated with experimental measurements[51]. Experimental final rotational state distributions for vibrationally **b** elastic ($v_f = 3$) and **c** inelastic ($v_f = 2$) scattering of NO($v_i = 3$) from Au(111) with $E_i = 0.96$ eV, for N-first and O-first orientations, compared with IESH results on the revPBE and PW91 PESs. IESH results for both channels are scaled to match the peaks of the experimental rotational state distributions. Source data are provided in a Source data file.

and corrugation of the PES, but their influences are coupled and subtle[52,53].

Both deficiencies likely stem from the insufficient accuracy of the PES in the entrance channel described by DFT based on the generalized gradient approximation (GGA). It is possible to take a specific reaction parameter (SRP) approach, which mixes the two density functionals to achieve a more balanced description of the molecule-surface interactions. This strategy has shown some success in accurately predicting experimental dissociation probabilities of H_2 on several metal surfaces[54,55]. However, its effectiveness in the current system is rather uncertain, because the mix of revPBE and PW91 functionals would unavoidably raise the barrier height compared to that of using PW91 alone and reduce the efficiency of VET. In addition, this strategy will unlikely improve the description of anisotropy and corrugation. More advanced hybrid functionals or doubly hybrid functionals beyond GGA have potential for attaining a systematically more accurate description of such systems[56,57], although at the price of much higher computational costs.

Besides the influence of molecule-surface interactions, the IESH method itself invokes approximations for describing a molecule interacting with an electron bath. First, IESH treats surface electrons independently[22], neglecting many-electron effects. Second, like other surface hopping methods, IESH also suffers from the overcoherence issue, although recent studies suggest its impact may be limited[38,58]. Nuclear quantum effects could also be significant in scattering processes involving sparse vibrational states[59]. These limitations may intricately influence the agreement with the experiment. Unfortunately, numerically exact quantum methods, such as HEOM, are computationally prohibitive for systems beyond 2D models[40]. Further research is needed to accurately benchmark the importance of many-electron and overcoherence effects in FD simulations. The PES training may also introduce additional errors to our model. However, given the small root mean square errors (RMSEs) and the good convergence behavior of the PESs (see Supplementary Note 2), we expect a minor influence of PES training errors on the simulation results.

Summarizing, this work reports a first-principles model within full dimensionality to investigate the VET dynamics in NO scattering from Au(111). In this model, two charge-transfer-related diabatic states of NO on Au(111) are calculated by CDFT, which are fitted to diabatic PESs by EANN. These PESs are then used to construct an effective Hamiltonian for the IESH nonadiabatic dynamics simulations, enabling the modeling of explicit electron transfer and EHP excitations on equal footing. A combination of these state-of-the-art techniques minimizes empirical parameters in the PESs and dynamical models typically involved in nonadiabatic simulations. This enables us to explicitly examine how the potential energy landscape simultaneously affects adiabatic and electron transfer mediated nonadiabatic energy transfer processes. Through systematic comparisons of previous 2D models and current FD models based on two different functionals, we find that both adiabatic and nonadiabatic energy transfer dynamics are dependent on the potential energy landscape and model dimensionality, which are crucial for quantitatively explaining experimental observations.

Our simulations also provide more convincing interpretations for some experimental observations that were not well understood. For instance, the dependence of the steric effect on the initial vibrational state was attributed to the change of the orientational dependence of metal-to-molecule electron transfer behavior as the molecule stretches. Additionally, our results indicate that during NO scattering, vibrational energy can couple to both surface electrons and molecular translation, whereas the direct coupling between molecular translation and surface electrons is negligible. In this regard, our PW91-based IESH model has achieved very good agreement with most experimental data, making a significant step towards a quantitatively accurate understanding of this benchmark system. This CDFT + EANN + IESH scheme scales reasonably with the system size, making it feasible to explore more complex chemical processes involving electron transfer on metal surfaces. Its general success in this model system will hopefully inspire further applications in hot electron-driven chemistry, which could provide first-principles insights into plasmonic photocatalysis[60,61].

Methods

CDFT calculations

A key difference between the present and a previous model[23] is that U_0 and U_1 are now determined by CDFT energies with a constrained Bader charge of 0 e^- and −1 e^- onto the NO moiety, respectively. Their couplings are then derived by their energies and the ground state DFT energy (E_g) via,

$$V_c = \sqrt{(U_0 - E_g) \times (U_1 - E_g)}, \tag{1}$$

which is then used to evaluate V_{ak}. According to Wu and Van Voorhis[44], in CDFT, the energy functional is defined by modifying the traditional DFT functional, $E[\rho]$, with a Lagrange multiplier (V) dependent on the charge constraint,

$$W[\rho, V] = E[\rho] + V\left(\int w_c(\mathbf{r})\rho(\mathbf{r})d\mathbf{r} - N_c\right). \tag{2}$$

Here, $w_c(\mathbf{r})$ is a spatial weight function of the charge density $\rho(\mathbf{r})$, and N_c is the target value of the charge constraint. The energy of the charge-constrained state is obtained by self-consistently minimizing W with respect to ρ and maximizing W with respect to V,

$$E_{CDFT} = \min_{\rho} \max_{V} [W[\rho, V]]. \tag{3}$$

The CDFT diabatic state energies and forces were obtained using the CDFT module implemented in CP2K[45]—a general way to calculate charge-constrained states for molecule-metal systems[46]. Compared to the electric field method[23], diabatic states defined by CDFT are well-behaved and smooth in the entire dynamically relevant configuration space, enabling constructions of FD diabatic PES with accuracy at the first-principles level. For the current NO/Au(111) system, the

convergence criterion for the charge constraint was set to 5×10^{-3} e$^-$. In detail, Kohn–Sham orbitals were expanded into a mixed Gaussian plane-wave basis, and the ionic cores were approximated by the Goedecker–Teter–Hutter (GTH) pseudopotentials[62]. Valence electrons were expanded with the DZVP-MOLOPT-SR-GTH basis set for all elements. Since NO is an open-shell molecule, all calculations were spin polarized. The surface was modeled by a 6×6 supercell with four metal layers. The top two layers of Au atoms were movable, and a vacuum space of 25 Å in the Z direction was used to separate the periodic slabs. A Fermi-Dirac smearing method was used with an electronic temperature of 1200 K to maintain the fractional occupation of states near the Fermi energy and to speed up self-consistent field convergence. Most calculations in this work have been done using the revPBE functional[63], except in some test calculations discussed below, where the PW91 functional[64] was used.

Ground and charge-transfer state PESs

EANN method. A well-established EANN method[65,66] was employed to learn CDFT energies and forces to yield charge-transfer state PESs, in the same way as representing the ground state PES. This allows us to construct the FD-IESH Hamiltonian without introducing any empirical parameters. In this approach, the total energy of the system is decomposed as the sum of atomic energies, each of which is represented by an atomic neural network,

$$E = \sum_{i=1}^{N} E_i = \sum_{i=1}^{N} NN_i(\rho^i), \tag{4}$$

where ρ^i are embedded atom density (EAD) features regarded as the input to each atomic neural network that can be simply expressed by the square of the linear combination of Gaussian-type orbitals (GTOs) located at neighbor atoms,

$$\rho^i = \sum_{l_x,l_y,l_z}^{l_x+l_y+l_z=L} \frac{L!}{l_x!l_y!l_z!} \left(\sum_{j\neq i}^{N_{\mathrm{cut}}} c_j^{Z_j} \varphi_{l_x l_y l_z}^{\alpha, r_s}(\mathbf{r}_{ij}) f_{\mathrm{c}}(\mathbf{r}_{ij}) \right)^2. \tag{5}$$

In Eq. (5), N_{cut} is the total number of neighbor atoms within a cutoff radius (r_{c}), $c_j^{Z_j}$ is the element-dependent orbital coefficient which can be optimized together with NNs parameters, and $f_{\mathrm{c}}(\mathbf{r}_{ij})$ is a cutoff function to ensure that the contribution of each neighbor atom decays smoothly to zero at r_{c}. The GTO, $\varphi_{l_x l_y l_z}^{\alpha, r_s}(\mathbf{r}_{ij})$, is defined by,

$$\varphi_{l_x l_y l_z}^{\alpha, r_s}(\mathbf{r}_{ij}) = x^{l_x} y^{l_y} z^{l_z} exp(-\alpha |r_{ij} - r_s|^2), \tag{6}$$

where $\mathbf{r}_{ij} = (x, y, z)$ is the Cartesian coordinates of the embedded atom i relative to a neighbor atom j, r_{ij} is its length, α and r_s are parameters that determine radial distributions of GTO, $l_x + l_y + l_z = L$ specifies the orbital angular momentum (L).

The revPBE-based PESs. It should be noted that we have constructed PESs based on two density functionals to investigate the influence of the energy landscape on the adiabatic and nonadiabatic VET dynamics. We first chose the revPBE functional[63] for two main reasons. First, IESH and HEOM results based on 2D (only includes the N–O bond length (r_{NO}) and the molecular height on the surface (Z_{NO}), as defined in Supplementary Fig. 1), PESs fitted from dozens of data points using the revPBE functional were available[40]. This allowed us to conveniently compare these results with our FD-IESH results to validate the accuracy of IESH and reveal the importance of multidimensional effects. Second, the revPBE functional predicts a binding energy of NO with Au(111) that agrees with the experimental value[67] (see Supplementary Table 1). However, as discussed above, the revPBE-based PESs appear too repulsive to enable efficient VET. Data points used to construct the revPBE-based ground, neutral, and anionic PESs were generated by two procedures. First, approximately 500 configurations for the NO/Au(111) system were randomly generated and computed to construct an initial ground state PES. The rest 2000 configurations were iteratively selected from quasi-classical trajectories on the iteratively refined ground state PES via both geometric and energetic criteria until the dynamical results converged. After excluding the non-converged configurations in DFT calculations, a total of 2285, 2165, 2047 data points were used to fit the ground, neutral, and anionic state EANN PESs, respectively, among which 90% of data points were used for training, while the remaining 10% were reserved for validation. These EANN hyperparameters take values of $L = 0$–2, $r_{\mathrm{c}} = 7.6$ Å, $\alpha = 0.53$ Å^{-2}, and $r_s = 0.0$–7.4 Å every 0.6 Å, yielding 39 EAD features. The atomic neural network comprises two hidden layers with 30 and 40 neurons for the ground, neutral, and anionic PESs. The overall RMSEs of the ground, neutral, and anionic PESs are 11.8, 59.9, and 75.8 meV for energies, and 17.7, 60.4, and 113.0 meV/Å for atomic forces, respectively. The significantly larger errors in the neutral and anionic state PESs compared to the ground state PES primarily stem from the broader energy range of diabatic states and extra errors in CDFT calculations.

The PW91-based PESs. While the potential energy landscape has been shown to critically regulate adiabatic energy transfer dynamics[32,49], its role in nonadiabatic energy transfer dynamics during molecule-metal scattering remains relatively unclear. Herein, we further construct diabatic state PESs using the PW91 functional, based on which BOMD predicted a large amount of vibrational energy loss after NO scattering from Au(111)[32,35]. As illustrated in Supplementary Note 1, the energy differences between the neutral and ground states (U_0–E_{g}) and between the anionic and ground states (U_1–E_{g}) calculated using the revPBE and PW91 functionals are very similar. To avoid performing costly CDFT calculations for thousands of configurations required for PES fitting, we add $(U_0^{\mathrm{RE}} - E_{\mathrm{g}}^{\mathrm{RE}})$ calculated on the revPBE PES on top of the PW91 ground state ($E_{\mathrm{g}}^{\mathrm{PW}}$) PES[32,35] reported previously to construct the PW91 neutral state (U_0^{PW}) PES,

$$U_0^{\mathrm{PW}} = E_{\mathrm{g}}^{\mathrm{PW}} + (U_0^{\mathrm{RE}} - E_{\mathrm{g}}^{\mathrm{RE}}). \tag{7}$$

The PW91 anionic state PES can also be obtained by,

$$U_1^{\mathrm{PW}} = E_{\mathrm{g}}^{\mathrm{PW}} + (U_1^{\mathrm{RE}} - E_{\mathrm{g}}^{\mathrm{RE}}), \tag{8}$$

where $(U_1^{\mathrm{RE}} - E_{\mathrm{g}}^{\mathrm{RE}})$ is the energy difference between the anionic and ground states calculated on the revPBE PES. These PW91-based PESs were subsequently applied in IESH simulations and compared with a variety of experiments.

IESH dynamics

In this work, nonadiabatic dynamics simulations for NO scattering from Au(111) are carried out by the IESH method[22,68]. The method is based on a discretized version of the Newns–Anderson (NA) Hamiltonian[69], which describes an impurity level (here the lowest unoccupied molecular orbital (LUMO) of the molecule) interacting with a manifold of electronic states with the assumption that the metallic electrons are non-interacting. The discretized many-electron NA Hamiltonian is written as,

$$\begin{aligned} H_{el}(\mathbf{R}) = U_0(\mathbf{R}) + (U_1(\mathbf{R}) - U_0(\mathbf{R}))\hat{a}^+\hat{a} + \sum_{k=1}^{M} \varepsilon_k \hat{c}_k^+ \hat{c}_k \\ + \sum_{k=1}^{M} V_{ak}(\mathbf{R})(\hat{a}^+\hat{c}_k + \hat{c}_k^+\hat{a}). \end{aligned} \tag{9}$$

Here, $U_0(\mathbf{R})$ is the PES for the interaction of a neutral molecule (with the LUMO orbital, $|a\rangle$, unfilled) with the metal surface, $U_1(\mathbf{R})$ is the PES

for the interaction of a negatively charged molecule (with $|a\rangle$ filled) with the metal surface, $\hat{a}^+(\hat{a})$ is the creation (annihilation) operator for an electron in $|a\rangle$. The third term in Eq. (9) describes non-interacting electrons, where $\hat{c}_k^+$ ($\hat{c}_k$) is the creation (annihilation) operator for the kth metal electron. The last term couples the molecular orbital and the metal orbital.

Due to the assumption of independent electrons, this Hamiltonian can be written as the sum of one-electron Hamiltonians, each of which is given by

$$H_{el}^1(\mathbf{R}) = (U_1(\mathbf{R}) - U_0(\mathbf{R}))|a\rangle\langle a| + \sum_{k=1}^{M} \varepsilon_k |k\rangle\langle k| + \sum_{k=1}^{M} V_{ak}(\mathbf{R})(|a\rangle\langle k| + |k\rangle\langle a|) \tag{10}$$

By diagonalizing Eq. (10), a series of eigenvalues (E_j) and eigenstates $|\varphi_j(\mathbf{R})\rangle$ are obtained. Thus, the adiabatic Hamiltonian for evolving the nuclear subsystem can be expressed with the eigenvalues,

$$H(\mathbf{R},\mathbf{P}) = \sum_{i=1}^{3N} \frac{P_i^2}{2M_i} + U_0(\mathbf{R}) + \sum_{j\in\mathbf{s}(t)} E_j(\mathbf{R}), \tag{11}$$

where the total energy of electrons is represented by the sum of a set of occupied single electronic states determined by a time-dependent vector $\mathbf{s}(t)$. The corresponding N_e-electron eigenstate of the many-electron Hamiltonian can then be obtained by populating N_e of these one-electron orbitals in a Slater determinant,

$$|\mathbf{j}\rangle = |\varphi_{j_1}\varphi_{j_2}, \ldots, \varphi_{j_{N_e}}|. \tag{12}$$

In this representation, the ground state corresponds to filling N_e (half of the number of metal orbitals, M) electrons from the lowest single-electron orbital up to the Fermi level, while the excited states correspond to the determinants in which one or more electrons jump to empty orbitals above the Fermi level.

In IESH, the total many-electron wave function is a single Slater determinant state,

$$|\Psi\rangle = |\psi_1\psi_2, \ldots, \psi_{N_e}|. \tag{13}$$

Each electron in the system is evolved independently according to the one-electron Hamiltonian H_{el}^1,

$$i\hbar\frac{\partial|\psi_\alpha\rangle}{\partial t} = H_{\mathrm{el}}^1(\mathbf{R})|\psi_\alpha\rangle, \tag{14}$$

where α goes from 1 to N_e. We expand each single-electron wave function in terms of $(M+1)$ electronic basis functions,

$$\psi_\alpha(\mathbf{r},\mathbf{R},t) = \sum_j c_j^\alpha(t)\varphi_j(\mathbf{r},\mathbf{R}), \tag{15}$$

where $\{c_j^\alpha\}$ are the complex expansion coefficients for the αth electron. Substituting Eq. (15) into Eq. (14), we get,

$$i\hbar\,\dot{c}_k^\alpha = E_k(\mathbf{R})\,c_k^\alpha - i\hbar\sum_{j\neq k}\dot{\mathbf{R}}\cdot\mathbf{d}_{kj}(\mathbf{R})\,c_j^\alpha, \tag{16}$$

where $\mathbf{d}_{kj}$ is the nonadiabatic coupling between orbitals k and j.

In practice, Eqs. (11) and (16) describe the evolution of the nuclear and electronic subsystems. Within the IESH approach, the hopping probability between electronic states represented by $|\mathbf{k}\rangle$ and $|\mathbf{j}\rangle$ is non-zero only when $|\mathbf{k}\rangle$ and $|\mathbf{j}\rangle$ differ in exactly one occupied orbital, that is, $k_1 = j_1, k_2 = j_2, \ldots, k_{Ne} = j_{Ne}$, except for a single orbital at which they differ ($k_i \neq j_i$). And the probability of a hop from the occupied orbital k to an unoccupied orbital j is calculated by,

$$g_{k\to j} = \max\left\{\frac{-2\,\mathrm{Re}(A_{kj})}{A_{kk}}\,\dot{\mathbf{R}}\cdot\mathbf{d}_{jk}\,\Delta t,\ 0\right\}, \tag{17}$$

where Δt is the electronic time step, A_{kj} and A_{kk} are elements of the electronic density matrix. After these modifications, the IESH method follows the conventional fewest-switch surface hopping algorithm[22,70].

Quasi-classical trajectory implementation

To compare with scattering experiments, we have performed quasi-classical trajectory calculations for the nuclear dynamics. The Jacobi coordinate frame of the NO/Au(111) system for describing the state-to-state scattering process is illustrated in Supplementary Fig. 1. The BOMD and IESH simulations were performed using an in-house modified version of the VENUS code[71,72]. In this work, all trajectories started with NO molecules positioned with the center of mass 8.0 Å above the topmost layer of Au(111), i.e., $Z_{NO} = 8.0$ Å (see Supplementary Fig. 1). The lateral coordinates of the center of mass of NO (X and Y) were randomly sampled in the simulation supercell. The initial polar (θ) and azimuthal (φ) angles of the molecular internuclear vector (defined as pointing from N to O) were randomly sampled unless stated otherwise. The initial values of the internuclear distance, r_{NO}, and the conjugated momentum were sampled semi-classically for given vibrational and rotational quantum numbers v and j[73]. The initial condition of surface atoms was chosen from the Anderson thermostat, but no thermostat was imposed during the collisional process. Nuclear coordinates and momenta were propagated using the Verlet algorithm with a time step of 0.1 fs, with a maximum simulation time of 10 ps. The trajectory was terminated and assigned to a "scattered" event when molecule-surface vertical distance exceeded 8.0 Å and the molecule velocity pointed away from the surface, for which the final vibrational state (v_f) of NO was determined by the Einstein–Brillouin–Keller quantization[74] and rotational quantum number (j_f) was obtained from the quantum mechanical expression for rotational angular momentum. Alternatively, the trajectory was labeled as "trapped" if the trajectory exceeded the maximum simulation time. To obtain the final rovibrational state distributions, the fractional vibrational and rotational quantum numbers were binned into the nearest integers via a histogram binning procedure.

Data availability

The training dataset and trained PESs generated in this study have been deposited in GitHub at https://github.com/gangm97/NO_Au111_scattering. Source data for all figures in the main text and Supplementary Information are provided in a Source data file. Source data are provided with this paper.

Code availability

The EANN code is available via GitHub at https://github.com/zhangylch/EANN. The heavily modified VENUS program is available from the corresponding author on request.

References

1. Rahinov, I. et al. Vibrational energy transfer in collisions of molecules with metal surfaces. *Phys. Chem. Chem. Phys.* **26**, 15090–15114 (2024).
2. Zhou, X., Meng, G., Guo, H. & Jiang, B. First-principles insights into adiabatic and nonadiabatic vibrational energy-transfer dynamics during molecular scattering from metal surfaces: the importance of surface reactivity. *J. Phys. Chem. Lett.* **13**, 3450–3461 (2022).
3. Werdecker, J., van Reijzen, M. E., Chen, B.-J. & Beck, R. D. Vibrational energy redistribution in a gas-surface encounter: state-to-state scattering of CH_4 from Ni(111). *Phys. Rev. Lett.* **120**, 053402 (2018).

4. Werdecker, J. et al. State-to-state methane-surface scattering as a probe of catalytic activity. *Phys. Rev. Res.* **2**, 043251 (2020).
5. Rettner, C. T., Auerbach, D. J., Tully, J. C. & Kleyn, A. W. Chemical dynamics at the gas-surface interface. *J. Phys. Chem.* **100**, 13021–13033 (1996).
6. Nieto, P. et al. Reactive and nonreactive scattering of H_2 from a metal surface is electronically adiabatic. *Science* **312**, 86–89 (2006).
7. Rahinov, I. et al. Quantifying the breakdown of the Born-Oppenheimer approximation in surface chemistry. *Phys. Chem. Chem. Phys.* **13**, 12680–12692 (2011).
8. Golibrzuch, K., Bartels, N., Auerbach, D. J. & Wodtke, A. M. The dynamics of molecular interactions and chemical reactions at metal surfaces: testing the foundations of theory. *Annu. Rev. Phys. Chem.* **66**, 399–425 (2015).
9. Alducin, M., Díez Muiño, R. & Juaristi, J. I. Non-adiabatic effects in elementary reaction processes at metal surfaces. *Prog. Surf. Sci.* **92**, 317–340 (2017).
10. Rettner, C. T., Fabre, F., Kimman, J. & Auerbach, D. J. Observation of direct vibrational excitation in gas-surface collisions: NO on Ag(111). *Phys. Rev. Lett.* **55**, 1904 (1985).
11. Beckerle, J. D., Casassa, M. P., Cavanagh, R. R., Heilweil, E. J. & Stephenson, J. C. Ultrafast infrared response of adsorbates on metal surfaces: vibrational lifetime of CO/Pt(111). *Phys. Rev. Lett.* **64**, 2090–2093 (1990).
12. Huang, Y., Wodtke, A. M., Hou, H., Rettner, C. T. & Auerbach, D. J. Observation of vibrational excitation and deexcitation for NO(*v*=2) scattering from Au(111): evidence of electron-hole pair mediated energy transfer. *Phys. Rev. Lett.* **84**, 2985 (2000).
13. Huang, Y., Rettner, C. T., Auerbach, D. J. & Wodtke, A. M. Vibrational promotion of electron transfer. *Science* **290**, 111–114 (2000).
14. White, J. D., Chen, J., Matsiev, D., Auerbach, D. J. & Wodtke, A. M. Conversion of large-amplitude vibration to electron excitation at a metal surface. *Nature* **433**, 503–505 (2005).
15. Cooper, R. et al. Multiquantum vibrational excitation of NO scattered from Au(111): quantitative comparison of benchmark data to ab initio theories of nonadiabatic molecule-surface interactions. *Angew. Chem. Int. Ed.* **51**, 4954–4958 (2012).
16. Christopher, P., Xin, H. & Linic, S. Visible-light-enhanced catalytic oxidation reactions on plasmonic silver nanostructures. *Nat. Chem.* **3**, 467–472 (2011).
17. Mukherjee, S. et al. Hot-electron-induced dissociation of H_2 on gold nanoparticles supported on SiO_2. *J. Am. Chem. Soc.* **136**, 64–67 (2014).
18. Wu, Q., Zhou, L., Schatz, G. C., Zhang, Y. & Guo, H. Mechanistic insights into photocatalyzed H_2 dissociation on Au clusters. *J. Am. Chem. Soc.* **142**, 13090–13101 (2020).
19. Stefancu, A., Halas, N. J., Nordlander, P. & Cortes, E. Electronic excitations at the plasmon–molecule interface. *Nat. Phys.* **20**, 1065–1077 (2024).
20. Monturet, S. & Saalfrank, P. Role of electronic friction during the scattering of vibrationally excited nitric oxide molecules from Au(111). *Phys. Rev. B* **82**, 075404 (2010).
21. Shenvi, N., Roy, S. & Tully, J. C. Dynamical steering and electronic excitation in NO scattering from a gold surface. *Science* **326**, 829–832 (2009).
22. Shenvi, N., Roy, S. & Tully, J. C. Nonadiabatic dynamics at metal surfaces: independent-electron surface hopping. *J. Chem. Phys.* **130**, 174107 (2009).
23. Roy, S., Shenvi, N. A. & Tully, J. C. Model Hamiltonian for the interaction of NO with the Au(111) surface. *J. Chem. Phys.* **130**, 174716 (2009).
24. Li, S. & Guo, H. Monte Carlo wave packet study of negative ion mediated vibrationally inelastic scattering of NO from the metal surface. *J. Chem. Phys.* **117**, 4499–4508 (2002).
25. Golibrzuch, K. et al. The importance of accurate adiabatic interaction potentials for the correct description of electronically non-adiabatic vibrational energy transfer: a combined experimental and theoretical study of NO(*v* = 3) collisions with a Au(111) surface. *J. Chem. Phys.* **140**, 044701 (2014).
26. Golibrzuch, K. et al. Incidence energy dependent state-to-state time-of-flight measurements of NO(*v* = 3) collisions with Au(111): the fate of incidence vibrational and translational energy. *Phys. Chem. Chem. Phys.* **16**, 7602–7610 (2014).
27. Bartels, N., Kruger, B. C., Auerbach, D. J., Wodtke, A. M. & Schafer, T. Controlling an electron-transfer reaction at a metal surface by manipulating reactant motion and orientation. *Angew. Chem. Int. Ed.* **53**, 13690–13694 (2014).
28. Golibrzuch, K. et al. State-to-state time-of-flight measurements of NO scattering from Au(111): direct observation of translation-to-vibration coupling in electronically nonadiabatic energy transfer. *J. Phys. Chem. A* **117**, 8750–8760 (2013).
29. Bartels, N. et al. Observation of orientation-dependent electron transfer in molecule-surface collisions. *Proc. Natl. Acad. Sci. USA* **110**, 17738–17743 (2013).
30. Cooper, R. et al. On the determination of absolute vibrational excitation probabilities in molecule-surface scattering: Case study of NO on Au(111). *J. Chem. Phys.* **137**, 064705 (2012).
31. Zhang, Y. et al. Stereodynamics of adiabatic and non-adiabatic energy transfer in a molecule surface encounter. *Phys. Chem. Chem. Phys.* **24**, 19753–19760 (2022).
32. Yin, R. & Jiang, B. Mechanical vibrational relaxation of NO scattering from metal and insulator surfaces: When and why they are different. *Phys. Rev. Lett.* **126**, 156101 (2021).
33. Box, C. L., Zhang, Y., Yin, R., Jiang, B. & Maurer, R. J. Determining the effect of hot electron dissipation on molecular scattering experiments at metal surfaces. *JACS Au* **1**, 164–173 (2021).
34. Serwatka, T., Füchsel, G. & Tremblay, J. C. Scattering of NO(*v* = 3) from Au(111): a stochastic dissipative quantum dynamical perspective. *Phys. Chem. Chem. Phys.* **22**, 6584–6594 (2020).
35. Yin, R., Zhang, Y. & Jiang, B. Strong vibrational relaxation of NO scattered from Au(111): importance of the adiabatic potential energy surface. *J. Phys. Chem. Lett.* **10**, 5969–5974 (2019).
36. Miao, G., Dou, W. & Subotnik, J. Vibrational relaxation at a metal surface: Electronic friction versus classical master equations. *J. Chem. Phys.* **147**, 224105 (2017).
37. Kruger, B. C. et al. no vibrational energy transfer on a metal surface: still a challenge to first-principles theory. *J. Phys. Chem. C* **119**, 3268–3272 (2015).
38. Gardner, J., Habershon, S. & Maurer, R. J. Assessing mixed quantum-classical molecular dynamics methods for nonadiabatic dynamics of molecules on metal surfaces. *J. Phys. Chem. C.* **127**, 15257–15270 (2023).
39. Malpathak, S. & Ananth, N. A linearized semiclassical dynamics study of the multiquantum vibrational relaxation of NO scattering from a Au(111) surface. *J. Phys. Chem. Lett.* **15**, 794–801 (2024).
40. Preston, R. J. et al. Nonadiabatic quantum dynamics of molecules scattering from metal surfaces. *J. Chem. Theory Comput.* **21**, 1054–1063 (2025).
41. Head-Gordon, M. & Tully, J. C. Molecular dynamics with electronic frictions. *J. Chem. Phys.* **103**, 10137–10145 (1995).
42. Dou, W. & Subotnik, J. E. Nonadiabatic molecular dynamics at metal surfaces. *J. Phys. Chem. A* **124**, 757–771 (2020).
43. Bartels, N. *Orientation-Dependent Energy Transfer in Gas-Surface Collisions: Scattering of Vibrationally Excited Nitric Oxide from Au(111).* Institute of Physical Chemistry, University of Göttingen (2015).
44. Wu, Q. & Van Voorhis, T. Direct optimization method to study constrained systems within density-functional theory. *Phys. Rev. A* **72**, 024502 (2005).

45. Holmberg, N. & Laasonen, K. Efficient constrained density functional theory implementation for simulation of condensed phase electron transfer reactions. *J. Chem. Theory Comput.* **13**, 587–601 (2017).
46. Meng, G. & Jiang, B. A pragmatic protocol for determining charge transfer states of molecules at metal surfaces by constrained density functional theory. *J. Chem. Phys.* **157**, 214103 (2022).
47. Meng, G. et al. First-principles nonadiabatic dynamics of molecules at metal surfaces with vibrationally coupled electron transfer. *Phys. Rev. Lett.* **133**, 036203 (2024).
48. Tanimura, Y. & Kubo, R. Time evolution of a quantum system in contact with a nearly Gaussian-Markoffian noise bath. *J. Phys. Soc. Jpn.* **58**, 101–114 (1989).
49. Meng, G., Hu, C. & Jiang, B. Vibrational relaxation of highly vibrationally excited molecules scattered from Au(111): role of the dissociation barrier. *J. Phys. Chem. C* **126**, 12003–12008 (2022).
50. Bartels, N. et al. Dynamical steering in an electron transfer surface reaction: oriented NO(v = 3, 0.08 <Ei <0.89 eV) relaxation in collisions with a Au(111) surface. *J. Chem. Phys.* **140**, 054710 (2014).
51. Wodtke, A. M., Yuhui, H. & Auerbach, D. J. Insensitivity of trapping at surfaces to molecular vibration. *Chem. Phys. Lett.* **413**, 326–330 (2005).
52. Kleyn, A. W., Luntz, A. C. & Auerbach, D. J. Rotational energy transfer in direct inelastic surface scattering: NO on Ag(111). *Phys. Rev. Lett.* **47**, 1169–1172 (1981).
53. Wang, Y., Yin, R. & Jiang, B. Rotationally inelastic scattering dynamics of NO from Ag(111): influence of interaction potentials. *J. Phys. Chem. C* **127**, 11966–11977 (2023).
54. Díaz, C. et al. Chemically accurate simulation of a prototypical surface reaction: H_2 dissociation on Cu(111). *Science* **326**, 832–834 (2009).
55. Nour Ghassemi, E., Wijzenbroek, M., Somers, M. F. & Kroes, G.-J. Chemically accurate simulation of dissociative chemisorption of D_2 on Pt(111). *Chem. Phys. Lett.* **683**, 329–335 (2017).
56. Gerrits, N. et al. Density functional theory for molecule–metal surface reactions: When does the generalized gradient approximation get it right, and what to do if it does not. *J. Phys. Chem. Lett.* **11**, 10552–10560 (2020).
57. Wang, Y. et al. Toward efficient and unified treatment of static and dynamic correlations in generalized Kohn–Sham density functional Theory. *JACS Au* **4**, 3205–3216 (2024).
58. Pradhan, C. S. & Jain, A. Detailed balance and independent electron surface-hopping method: the importance of decoherence and correct calculation of diabatic populations. *J. Chem. Theory Comput.* **18**, 4615–4626 (2022).
59. De, P. K. & Jain, A. Metal-induced fast vibrational energy relaxation: quantum nuclear effects captured in diabatic independent electron surface hopping (IESH-D) method. *J. Phys. Chem. A* **127**, 4166–4179 (2023).
60. Zhang, Y. et al. Surface-plasmon-driven hot electron photochemistry. *Chem. Rev.* **118**, 2927–2954 (2018).
61. Martirez, J. M. P., Bao, J. L. & Carter, E. A. First-principles insights into plasmon-induced catalysis. *Annu. Rev. Phys. Chem.* **72**, 99–119 (2021).
62. Hartwigsen, C., Goedecker, S. & Hutter, J. Relativistic separable dual-space Gaussian Pseudopotentials from H to Rn. *Phys. Rev. B* **58**, 3641–3662 (1998).
63. Zhang, Y. & Yang, W. Comment on "Generalized gradient approximation made simple". *Phys. Rev. Lett.* **80**, 890–890 (1998).
64. Perdew, J. P. et al. Atoms, molecules, solids, and surfaces: applications of the generalized gradient approximation for exchange and correlation. *Phys. Rev. B* **46**, 6671–6687 (1992).
65. Zhang, Y., Hu, C. & Jiang, B. Embedded atom neural network potentials: Efficient and accurate machine learning with a physically inspired representation. *J. Phys. Chem. Lett.* **10**, 4962–4967 (2019).
66. Zhang, Y., Lin, Q. & Jiang, B. Atomistic neural network representations for chemical dynamics simulations of molecular, condensed phase, and interfacial systems: efficiency, representability, and generalization. *WIREs Comput. Mol. Sci.* **13**, e1645 (2023).
67. Engelhart, D. P., Wagner, R. J. V., Meling, A., Wodtke, A. M. & Schäfer, T. Temperature programmed desorption of weakly bound adsorbates on Au(111). *Surf. Sci.* **650**, 11–16 (2016).
68. Shenvi, N. & Tully, J. C. Nonadiabatic dynamics at metal surfaces: independent electron surface hopping with phonon and electron thermostats. *Faraday Discuss.* **157**, 325–335 (2012).
69. Newns, D. M. Self-consistent model of hydrogen chemisorption. *Phys. Rev.* **178**, 1123 (1969).
70. Tully, J. C. Molecular dynamics with electronic transitions. *J. Chem. Phys.* **93**, 1061–1071 (1990).
71. Hu, X., Hase, W. L. & Pirraglia, T. Vectorization of the general Monte Carlo classical trajectory program VENUS. *J. Comput. Chem.* **12**, 1014–1024 (1991).
72. Hase, W. L. et al. VENUS96: a general chemical dynamics computer program. *Quantum Chem. Program Exch. Bull.* **16**, 671 (1996).
73. Hase, W. L. Classical trajectory simulations: initial conditions. in *Encyclopedia of Computational Chemistry* (ed. Alinger, N. L.) (Wiley, 1998).
74. Gutzwiller, M. C. *Chaos in Classical and Quantum Mechanics* (Springer, 1990).

Acknowledgements

This work is supported by the Innovation Program for Quantum Science and Technology (grant no. 2021ZD0303301 to B.J.), the Strategic Priority Research Program of the Chinese Academy of Sciences (grant no. XDB0450101 to B.J.), National Natural Science Foundation of China (grant nos. 22325304 and 22221003 to B.J.). Dynamics simulations and model training were performed on the robotic AI-Scientist platform of the Chinese Academy of Sciences. The authors sincerely thank Profs. Alec Wodtke, Tim Schäfer, Hua Guo, Reinhard Maurer, and Wenjie Dou, Dr. Yaolong Zhang, and Mr. Junyang Hong for their insightful discussions.

Author contributions

B.J. designed the project and led the supervision of this research. G.M. wrote the code and performed all calculations. G.M. and B.J. wrote the manuscript.

Competing interests

The authors declare no competing interests.

Additional information

Supplementary information The online version contains supplementary material available at https://doi.org/10.1038/s41467-025-65513-5.

Correspondence and requests for materials should be addressed to Bin Jiang.

Peer review information *Nature Communications* thanks Daniel Auerbach and the other, anonymous, reviewers for their contribution to the peer review of this work. A peer review file is available.